International Journal of Thermal Sciences 162 (2021) 106789

Contents lists available at ScienceDirect

International Journal of Thermal Sciences

journal homepage: http://www.elsevier.com/locate/ijts

Large eddy simulation of natural convection heat transfer and fluid flow around a horizontal cylinder

Haiteng Ma [a,*], Li He [b]

[a] School of Mechanical Engineering, Shanghai Jiao Tong University, Shanghai, 200240, China
[b] Department of Engineering Science, University of Oxford, Oxford, OX2 0ES, UK

ARTICLE INFO

Keywords:
Natural convection heat transfer
Large eddy simulation
Buoyant plume
Computational fluid dynamics
Horizontal cylinder

ABSTRACT

Natural convection around a single horizontal cylinder has been extensively studied for heat transfer characteristics, but when coupled with fluid flow, the laminar-to-turbulent transition in buoyant plume poses severe challenge on modelling fidelity and physical interpretability. To address this challenge, this paper conducts detailed verification, validation and analysis of high-fidelity large eddy simulation (LES) for an unconfined horizontal cylinder in water with a Rayleigh number of 8×10^7, complemented by Reynolds-Averaged Navier-Stokes (RANS) computations. To the best of the authors' knowledge, this is the first LES study with acceptable accuracy as validate by experimental data for buoyant plume above a single horizontal cylinder. It is found that LES is far more sensitive to mesh resolution and boundary condition setting than RANS. An alarm is set for the use of periodic condition in LES on lateral boundaries of computational domain due to its inferior accuracy than RANS with transition SST model. The finely-tuned LES with pressure condition on lateral boundaries shows satisfactory agreement with experimental data in terms of heat transfer on cylinder surface and buoyant plume velocity, based on which new physical insight on transitional behavior of thermal plume is obtained. It is found that after leaving the cylinder, buoyant plume is laminar and accelerates, subject to work input from buoyancy force, while its temperature keep decreasing due to heat loss to atmosphere. Flow instability appears first in upward velocity at a streamwise Grashof number of 1.5×10^8, where transition to turbulence onsets. Thermal plume continues to accelerate until it begins to sway horizontally, where energy dissipation into turbulence becomes the major loss mechanism of mean flow energy. Thus, cross-stream diffusivity is augmented notably due to turbulent stresses, leading to smoothing of transverse velocity distribution and reduction of transversely-averaged mean kinetic energy. Transversely-averaged turbulent kinetic energy keeps increasing in transitional regime until the streamwise Grashof number reaches 7×10^9 and then declines to approach an asymptotic value, signifying the end of transition. Overall speaking, buoyancy work dominates the change in mean flow energy, while mean shear outweighs buoyancy in producing turbulent kinetic energy.

1. Introduction

Natural convection is important for a wide range of applications in energy sector, such as passive heat exchanger, submerged pipelines, HVAC system and electronic cooling. In many engineering practices, free convection has the potential to supplant forced convection driven by mechanical fans or other active fluid circulation machines, contributing to power saving, noise reduction and enhanced operational reliability. Examples include the subsea cooler developed by Gyles et al. [1] and thermal chimney described in Ma et al. [2] and Burnside et al. [3]. In the design and analysis of these systems, heat transfer and fluid flow interaction of natural convection plays a crucial role.

Researches on natural convection around horizontal cylinders have primarily focused on heat transfer characteristics for many decades. Much of the effort has been devoted to obtaining empirical correlation between Nusselt number and Rayleigh number, which is used in heat exchanger design extensively. For free convection of a single horizontal cylinder, such heat transfer correlations were reported from the experiments by Morgan [4], Churchill and Chu [5] and more recently by Atayılmaz and Teke [6].

Despite simplicity in geometry, natural convection fluid flow around a single horizontal cylinder is actually very complicated, because the

* Corresponding author.
E-mail address: haiteng.ma@sjtu.edu.cn (H. Ma).

https://doi.org/10.1016/j.ijthermalsci.2020.106789
Received 24 June 2020; Received in revised form 4 November 2020; Accepted 1 December 2020
Available online 16 December 2020
1290-0729/

buoyant plume is prone to instability and will transit to turbulence as it develops, as presented in the experiments of Carlomagno et al. [7] and Kitamura et al. [8]. Flow transition to turbulence greatly enhances heat transfer on cylinder surface, for the case of a single cylinder (Kitamura et al. [9]), two vertically-aligned cylinders (Grafsrønningen and Jensen [10]) and a vertical column of multiple cylinders (Kitamura et al. [8]). Thus, understanding transitional behavior of thermal plume is significant for both fluid dynamics and heat transfer investigations.

Compared to profuse heat transfer data, researches on fluid dynamics of thermal plume above a horizontal cylinder, particularly the transition mechanism, is relatively insufficient and attracting attention only in recent yeats. For an unconfined horizontal cylinder, Grafsrønningen et al. [11] conducted detailed particle image velocimetry (PIV) measurements of buoyant plume and derived turbulent production and Reynolds stress at Rayleigh numbers from 2.05×10^7 to 7.94×10^7. They concluded that the transitional location seems to travel upstream towards the cylinder as Rayleigh number increases. Similar conclusion is also presented by Grafsrønningen and Jensen [12] from simultaneous PIV and laser induced fluorescence (LIF) measurements. For a single cylinder in water tank with a free surface, velocity measurements have been presented by Atmane et al. [13] and Kuehner et al. [14,15]. They reported that buoyant plume can be unstable and exhibits swaying and meandering motions, which induce penetrative convection and in turn, sustains plume swaying, causing oscillations in cylinder heat transfer. For very simple or even idealized geometries, several studies have investigated the transitional behavior of buoyant plume, such as for a point heat source (Kimura and Bejan [16]), a line heat source (Noto et al. [17]), and a circular disk (Elicer-Cortes et al. [18,19]). However, for an unconfined horizontal cylinder which is representative of bare tube heat exchanger used in Gyles et al. [1], knowledge about flow physics of transitional buoyant plume is still inadequate and needs to be promoted.

In addition to the above experimental studies, computational fluid dynamics (CFD) of natural convection heat transfer on a horizontal cylinder have been implemented extensively using the simplest laminar flow model. Some classic numerical work has been adopted as benchmark solution for various Rayleigh and Prandtl numbers (Kuehn and Goldstein [20], Wang et al. [21] and Saitoh et al. [22]). Laminar model works reasonably well for flow around the heated horizontal cylinder except near trailing edge, where the formation of thermal plume nullifies boundary layer assumption and incurs large discrepancy with experimental data. A recent study by Atayılmaz and Teke [6] found their experimental data and numerical results of Nusselt number deviate within a $\pm$ 20% band. Due to the simple geometry and abundance of data available, natural convection around a single horizontal cylinder has been used by many researchers to validate their computational solver. They all reported good agreement with experimental Nusselt number, and then continued to study more complex configurations, such as cylinder with horizontal confinement (Sebastian and Shine [23], Lin et al. [24], Kumar et al. [25]), cylinder array (Corcione [26]), two attached cylinders (Liu et al. [27]), finned tube (Kumar et al. [28]),and even viscoplastic or Carreau fluids (Kefayati and Tang [29–33]), using the laminar model.

Computation of natural convection fluid flow is greatly challenged by the fact that transition from laminar to turbulent flow will occur as buoyant plume above a heated cylinder evolves. Several turbulence models have been proposed over the years for a broad range of applications, including Reynolds-Averaged Navier-Stokes (RANS), large eddy simulation (LES) and direct numerical simulation (DNS) (Pope [34]).

DNS solves the Navier-Stokes equations directly and resolves all the scales of motion. It has unrivalled accuracy but extremely high computational cost. As an example, for a pure thermal plume from a 2D ring disk studied by Pham et al. [35], the mesh resolution in DNS is 200 times finer than LES, while the time step is about 10 time smaller. Thus DNS is virtually infeasible for engineering application even with recent advances in computing power. Therefore, this paper will focus on the other two turbulence modelling techniques which are more practically viable.

In RANS, turbulence stress terms are modelled through transport equations or viscosity hypothesis, in order to form a closure to the Reynolds equations of mean flow variables. This steady flow method has been so far successfully applied to a wide range of industries, and will also be an indispensable tool in the coming decade (Slotnick et al. [36]). It is the most common and mature method, with numerous closure models derived for various scenarios. Specifically for transitional flows, a correction-based model (Menter et al. [37]) and a three-equation eddy-viscosity model based on k-ω framework (Walters and Cokljat [38]) have been successfully applied in engineering practices and integrated into commercial solvers in the last decade. However, the main limitation of RANS is all turbulent scales are modelled rather than resolved. Hence, its accuracy and reliability will be undermined.

For free convection of a horizontal cylinder, some researchers stated that RANS models predict the surface Nusselt number reasonably well compared with existing correlations or experimental data (Farouk and Güceri [39] and Pelletier et al. [40]). Furthermore, Pelletier et al. [40] found RANS model results exhibit good agreement with experimental data in heat transfer of two vertically-aligned cylinders, indicating the mean effect of buoyant plume on downstream cylinder is simulated reliably. For more complex geometries like fin and tube heat exchangers, Chen et al. [41–45] demonstrated that RANS models, including $k-\varepsilon$ RNG and zero-equation turbulence model, outperforms laminar model in terms of matching experimental temperature and heat transfer data. But according to Grafsronningen and Jensen [46], computations with several RANS models all overpredict the upward velocity and temperature excess in the transitional buoyant plume greatly. Thus, predictive reliability of RANS models is questionable, especially for thermal plume which undergoes transition to turbulence.

The deficiency of RANS is amended by LES, which solves the filtered equations of motion whose length scale is larger than the filter size, while only the more isotropic small scale turbulence is modelled. It has shown superior accuracy over RANS, especially for flow that is intrinsically unstable or unsteady, such as trailing edge vortex in turbomachinery (Léonard et al. [47]). However, computational cost of LES is much heavier than RANS, which is typically two orders of magnitude higher, impeding its application scope for the foreseeable future (Slotnick et al. [36]). As a result, the realm of LES (as in 2015) is divided into two categories: on one hand, the academic community considers properly resolved LES for idealized configurations, while on the other hand, the industrial community deals with under-resolved LES of more realistic geometries (Gourdain et al. [48]).

It should be noted that CFD accuracy is dictated by many factors, including modelling, boundary condition setting, mesh adequacy and numerics (temporal and spatial discretization), as stated by Denton [49]. Moving from RANS to LES only contributes to lower error in turbulence modelling part. As it often turns out, a poorly resolved high-fidelity computation can easily produce worse and more inconsistent results than a low-fidelity one would, argued by He and Yi [50]. It has been shown by Léonard et al. [47] that boundary layer velocity profiles are better predicted by RANS than LES on a voluntary coarse grid, indicating that LES is more sensitive to grid refinement. In fact, the trade-off between modelling effort and other CFD ingredients (mesh resolution, boundary condition, etc.), as well as its influence on the quality of simulations is not trivial at all.

LES of buoyant plume above a heated horizontal cylinder has rarely been carried out. To the best of the authors' knowledge, the only related work is presented by Grafsrønningen and Jensen [51], and their numerical results show considerable discrepancy with their previously reported experimental data (Grafsrønningen and Jensen [12]). Although quite a lot numerical setups had been modulated as an attempt to match experimental data, plume center velocity is still highly overestimated, while the plume width is also wrongly computed. Nevertheless, LES has shown good performance in estimating turbulence statistics of free convection thermal plume for more idealized geometries such as a line

heat source (Bastiaans et al. [52]) or a 2D ring disk (Pham et al. [35]). Therefore, computational reliability of LES in free convection around a horizontal cylinder needs to be ameliorated.

This paper aims to investigate the physical mechanism that governs the development of buoyant plume above a single horizontal cylinder, with a special focus on transitional behavior, by means of LES whose fidelity is greatly improved compared to the state of the art. LES study is conducted for a single horizontal cylinder in water at a Rayleigh number of 8×10^7, complemented by RANS computations. Numerical sensitivity of LES to time step size, ensemble-averaging period, mesh resolution and boundary condition is tested thoroughly. CFD results are then validated against the experimental data of Grafsrønningen et al. [11] in terms of Nusselt number on cylinder surface and velocity evolution in buoyant plume. Next, the well-calibrated LES results are analyzed to reveal mean flow and turbulence characteristics of buoyant plume. Transition of buoyant plume is identified and analyzed. Physical mechanisms that drive the development of transitional buoyant plume is finally elucidated from the budget analysis of kinetic energy for mean flow and turbulence.

2. Computational method, verification and validation

Computational models in this paper are set to match the experimental study of Grafsrønningen et al. [11] whenever possible. To recap the experimental study, a heated horizontal cylinder with an outer diameter (D) of 54 mm is submerged in a large water tank, which has a water depth of 1.6 m and 1.2 m in width and length. Thus the cylinder can be regarded as unconfined. Cylinder is heated with a uniform heat flux of 11.1 kW/m^2, offering a Rayleigh number of 7.94×10^7. Here, Rayleigh number is calculated using wall temperature and fluid properties in film temperature ($T_f = (T_w + T_\infty)/2$) at 90°peripheral angle.

2.1. Numerical method

2.1.1. Theoretical formulations

To resolve natural convection heat transfer and fluid flow, the following assumptions are made in this study:

(1) Fluid is Newtonian, i.e. fluid viscosity is independent of the shear rate, such as water, air.
(2) . This assumption, called Boussinesq approximation, is a commonly used approach in buoyant simulations. It is valid when the relative density change is small, i.e. $\Delta\rho/\rho = \beta\Delta T \ll 1$. In the present study, the relative density change is 0.006. Besides, Gray and Giorgini [53] concluded that Boussinesq approximation is valid in water as long as Rayleigh number is smaller than 10^{19}. Hence, application of Boussinesq approximation in the present study is justifiable.

Dimensional form of Navier-Stokes equations with Boussinesq approximation, which is also referred to as Boussinesq equations, is then denoted as:

$$\frac{\partial u_i}{\partial x_i} = 0 \tag{1}$$

$$\frac{\partial u_i}{\partial t} + u_j\frac{\partial u_i}{\partial x_j} = -\frac{1}{\rho}\frac{\partial p}{\partial x_i} + \frac{\partial}{\partial x_j}\left(\nu\frac{\partial u_i}{\partial x_j}\right) + \beta g_i \Delta T \tag{2}$$

$$\frac{\partial T}{\partial t} + u_j\frac{\partial T}{\partial x_j} = \frac{\partial}{\partial x_j}\left(\alpha\frac{\partial T}{\partial x_j}\right) \tag{3}$$

, where $\Delta T = T - T_\infty$ and β is thermal expansion coefficient (1/K).

To non-dimensionalize the governing equations, following dimensionless variables are introduced:

$$u_i^* = \frac{u_i}{U_0}, t^* = \frac{U_0 t}{L}, x_i^* = \frac{x_i}{L}, \Delta T^* = \frac{\Delta T}{\Delta T_0}, p^* = \frac{p}{\rho U_0^2} \tag{4}$$

, where characteristic length, velocity and temperature difference is L, U_0 and ΔT_0. Substituting Equation (4) into Equations (1)–(3), and dropping asterisk,

$$\frac{\partial u_i}{\partial x_i} = 0 \tag{5}$$

$$\frac{\partial u_i}{\partial t} + u_j\frac{\partial u_i}{\partial x_j} = -\frac{\partial p}{\partial x_i} + \frac{\nu}{U_0 L}\frac{\partial^2 u_i}{\partial x_j^2} + \frac{L}{U_0^2}\beta g_i \Delta T_0 \Delta T \tag{6}$$

$$\frac{\partial T}{\partial t} + u_j\frac{\partial T}{\partial x_j} = \frac{\alpha}{U_0 L}\frac{\partial^2 T}{\partial x_j^2} \tag{7}$$

In the present case, characteristic length (L) is selected as the cylinder diameter (D), characteristic velocity $U_0 = \sqrt{g\beta D\Delta T_0}$, and characteristic temperature difference $\Delta T_0 = T_{\theta=90^\circ} - T_\infty$ where $T_{\theta=90^\circ}$ is wall temperature at a circumferential angle of 90° on cylinder surface. Equations (5)–(7) is rewritten as,

$$\frac{\partial u_i}{\partial x_i} = 0 \tag{8}$$

$$\frac{\partial u_i}{\partial t} + u_j\frac{\partial u_i}{\partial x_j} = -\frac{\partial p}{\partial x_i} + \frac{1}{\sqrt{Ra/Pr}}\frac{\partial^2 u_i}{\partial x_j^2} + \Delta T\delta_{i2} \tag{9}$$

$$\frac{\partial T}{\partial t} + u_j\frac{\partial T}{\partial x_j} = \frac{1}{\sqrt{Ra\cdot Pr}}\frac{\partial^2 T}{\partial x_j^2} \tag{10}$$

where Rayleigh number $Ra = \sqrt{\frac{g\beta D^3\Delta T_0}{\nu\alpha}}$ and Prandtl number $= \frac{\nu}{\alpha}$.

To resolve turbulent flows in buoyant plume, large eddy simulations (LES) are implemented in this paper. Its theoretical principle is splitting a generic turbulent variable f into a large scale component $\bar{f}$ and a subgrid component f' (Bastiaans et al. [52]), denoted as,

$$f(x_i, t) = \bar{f}(x_i, t) + f'(x_i, t) \tag{11}$$

$$\bar{f}(x_i, t) = \int_\Omega g(x_i - x_i')f(x_i', t)dx_i' \tag{12}$$

where the filter function g satisfy the normalization condition,

$$\int_\Omega g(x_i - x_i')dx_i' = 1 \tag{13}$$

Executing the filtering operation to governing equations yields a depiction of large scale motion in turbulence as,

$$\frac{\partial \overline{u_i}}{\partial x_i} = 0 \tag{14}$$

$$\frac{\partial \overline{u_i}}{\partial t} + \overline{u_j}\frac{\partial \overline{u_i}}{\partial x_j} = -\frac{\partial \bar{p}}{\partial x_i} + \frac{1}{\sqrt{Ra/Pr}}\frac{\partial^2 \overline{u_i}}{\partial x_j^2} + \overline{\Delta T}\delta_{i2} - \frac{\partial \tau_{ij}}{\partial x_j} \tag{15}$$

$$\frac{\partial \overline{T}}{\partial t} + \overline{u_j}\frac{\partial \overline{T}}{\partial x_j} = \frac{1}{\sqrt{Ra\cdot Pr}}\frac{\partial^2 \overline{T}}{\partial x_j^2} - \frac{\partial h_j}{\partial x_j} \tag{16}$$

In the filtered governing equations, unresolved stress in momentum equation and heat flux in energy equation describe interaction between resolved large scale field and the small scale one. They are defined and calculated through gradient diffusion concept as,

$$\tau_{ij} = \overline{u_i u_j} - \overline{u_i}\cdot\overline{u_j} = -2\nu_t \overline{S_{ij}} \tag{17}$$

$$h_j = \overline{u_j T} - \overline{u_j} \cdot \overline{T} = -\alpha_t \frac{\partial \overline{T}}{\partial x_j} \tag{18}$$

where the filtered rate-of-strain tensor $\overline{S_{ij}} = \frac{1}{2}\left(\frac{\partial \overline{U_i}}{\partial x_j} + \frac{\partial \overline{U_j}}{\partial x_i}\right)$. Ratio between subgrid eddy viscosity (ν_t) and subgrid eddy diffusivity (α_t) is defined as turbulent Prandtl number ($Pr_t = \nu_t/\alpha_t$). It typically lies within $1/3 < Pr_t < 1/2$, as stated by Eidson [54]. When turbulent Prandtl number is given, only the subgrid eddy viscosity needs to be modelled in terms of resolved flow variables.

To account for turbulent stress that is not resolved in the filtered governing equations, Subgrid-scale (SGS) model is developed. The most classical SGS model is the Smagorinsky model ([55]) given by

$$\nu_t = C_s \Delta^2 \left|\overline{S}\right| \tag{19}$$

, where characteristic filtered rate of strain $\left|\overline{S}\right| = (2\overline{S_{ij}} \cdot \overline{S_{ij}})^{1/2}$, Δ is the filter size and $C_s = 0.0289$.

The problem with classical Smagorinsky model is appropriate value of C_s is not constant in different flow regimes (Pope [34]). For instance, C_s is zero in laminar flow, and it becomes smaller than 0.0289 close to solid walls. To overcome this issue, dynamic Smagorinsky model is developed by Germano et al. [56]. Here, C_s is dynamically computed through the resolved scales of motion. Its basic concept is to apply a second filter (called the test filter) to the governing equations. Both the grid filter and test filter generate a resolved flow field. Difference between the two resolved fields is the contribution of the small scales whose size is between the two filters, which can be used to compute C_s. This procedure is denoted as,

$$C_s = \frac{1}{2}\frac{L_{ij}M_{ij}}{M_{kl}M_{kl}} \tag{20}$$

, where $L_{ij} = \widehat{\overline{u_i}\overline{u_j}} - \widehat{\overline{u_i}}\widehat{\overline{u_j}}$ and $M_{ij} = \Delta^2 \widehat{\left|\overline{S}\right|\overline{S_{ij}}} - \widehat{\Delta}^2 \left|\widehat{\overline{S}}\right| \widehat{\overline{S_{ij}}}$. The hat operator $\widehat{\ }$ denotes a low-pass filtering with a kernel size of $\widehat{\Delta} = 2\Delta$.

Superior performance of dynamic model over the static one in capturing transition of thermal plume with jet inflow has been presented by Worthy [57]. Thus, the present study uses dynamic Smagorinsky model as the SGS model to represent small-scale turbulence.

2.1.2. Numerical domain, mesh and boundary conditions

Computational domain and mesh employed in the current study are shown in Fig. 1. The domain has a width of 20D with the cylinder in the middle, and a height of 30D, with the cylinder located at 10D above the bottom. In the spanwise x_3-direction, a domain depth of 4D is chosen according to the previous LES of Grafsrønningen and Jensen [51].

Grid resolution is significant in LES because it dictates the filter size, which should be small enough to resolve 80% of the energy so that the remaining 20% is modelled, according to Pope [34]. The filter size $\Delta = V^{1/3}$, where V is the volume of the computational cell. Kolmogorov length scale, which characterizes the smallest eddies in turbulence normally, is calculated as $\eta = (\nu^3/\varepsilon)^{1/4} \approx Gr^{(-3/8)}D$, where Gr is the Grashof number. But in thermal flows with Prandtl number larger than 1, Batchelor [58] stated that the conduction cut-off scale becomes the smallest, which is $\eta_B = (\nu\alpha^2/\varepsilon)^{1/4} \approx Gr^{(-3/8)}Pr^{(-1/2)}D$, where Pr is the Prandtl number. In this study, $\eta = 0.11$ mm, $\eta_B = 0.04$ mm. The grid resolution in the plume region is determined accordingly. The mesh has 176 nodes on the circumference of the cylinder and 50 nodes on the spanwise x_3-direction. Grid normal to cylinder surface is graded to a minimum spacing of 0.01 mm with an expansion ratio of 1.1, in order to resolve the near-wall boundary layer. The mesh grid has a total number of 6,245,000 nodes, determined from the mesh sensitivity study in Section 2.2.3.

Boundary condition on the cylinder is specified as no-slip wall with a constant heat flux of 11.1 kW/m^2, in accordance with experiment by Grafsrønningen et al. [11]. On the bottom boundary of the domain, pressure inlet with a total pressure of 1 atm at room temperature (293 K) is specified. Pressure outlet with a static pressure of 1 atm is specified on the top boundary and on lateral boundaries (highlighted in Fig. 1) unless otherwise stated. Such boundary condition settings have been used successfully by Heo et al. [59] and Sebastian and Shine [23]. Comparative study of using periodic condition on lateral boundaries will be described later in this paper. Periodic boundary condition is assigned in the spanwise x_3-direction.

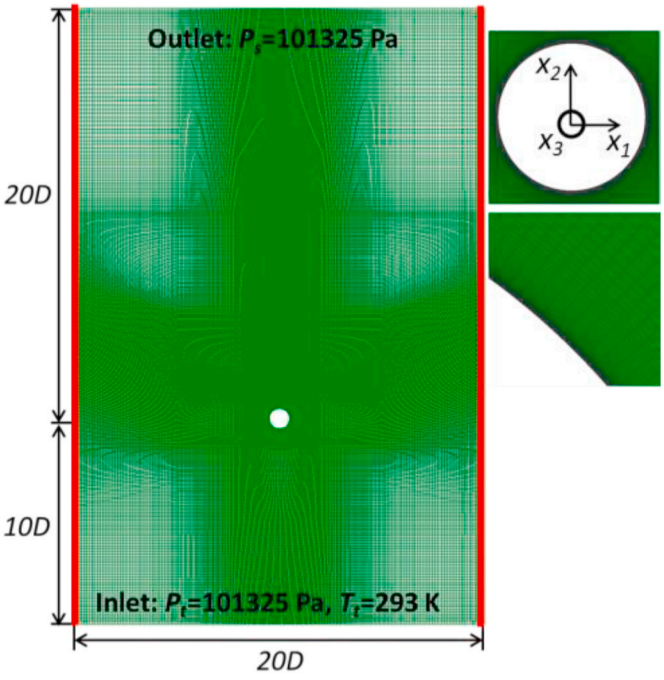

Fig. 1. Computation domain and mesh (lateral boundaries highlighted in red).

2.1.3. Numerical algorithm and solver

Numerical computations are carried out in ANSYS Fluent 19.0 commercial package. A pressure based solver is employed and the pressure-velocity coupling scheme is SIMPLEC. Acceleration along vertical x_2-axis is set as -9.8 m^2/s^2 to include the gravity effect. Spatial discretization of pressure and gradient is conducted by body force weight and least squares cell based scheme, respectively. Spatial discretization of momentum and energy equation is approached by bounded central differencing and second order upwind scheme. Time marching is achieved by bounded second order implicit scheme. Details of solver algorithm and discretization scheme are documented in ANSYS Fluent Theory Guide.

LES computation is run on 16 CPU cores by parallel, and takes an elapsed time of 50 h (or a total CPU time of 800 h) for one typical case, with a grid size of 6.25 million and a time step size of 0.05 s.

Water properties are evaluated at 293 K and 1 atm based on the table from NIST Reference Fluid Thermodynamic and Transport Properties Database (REFPROP).

For the purpose of comparison, RANS computations are also implemented on the same computational domain as LES. A two-dimensional mesh is adopted in RANS because mean flow variables in the spanwise x_3-direction are basically the same. The structured two-dimensional mesh has 125,000 nodes in total. Mesh independence study has been carried out and detailed in Section 2.2.3. Boundary conditions and solver settings are the same as LES unless otherwise stated. Six RANS models are tested: k-ε realizable, k-ε RNG, k-ω SST, transition-k-kl-ω, transition SST and Reynolds stress model.

2.2. Numerical sensitivity

2.2.1. Time step independence

To determine the time step size, Fig. 2 shows velocity magnitude (U) at centerline ($\times_1 = 0$) along the vertical x_2-axis for three time steps in LES. As the time step (Δt) reduces from 0.05 s to 0.01 s, the change in velocity magnitude is conspicuously smaller than that when the time step reduces from 0.1 s to 0.05 s. The maximum difference with respect to the smallest time step is 4.8% for $\Delta t = 0.05$ s and 7.8% for $\Delta t = 0.1$ s. Thus, a time step of $\Delta t = 0.05$ s is adequately precise and selected.

2.2.2. Influence of ensemble average period

Initial condition in LES is taken from steady RANS solution with transition SST model, which is shown to be the best among RANS models investigated in Section 2.3. After running the simulation for a physical time of 50 s, the effect of initialization could be removed and the flow enters statistically stationary state. Solution continues for another physical period of 100 s or 200 s to do ensemble averaging. It is worth noting that one flow-through time in this study is 33 s, based on the domain extent and characteristic velocity (U_0). So the ensemble-average time period corresponds to 3 or 6 flow through. Its influence on the velocity development at centerline is illustrated in Fig. 3. As it turns out, only minor difference is observed between the two, with a maximum difference of 3% occurring at x_2/D = 2.4. Thus, an ensemble-averaging time of 100 s (3 flow through) is considered adequate.

2.2.3. Mesh independence

To compare mesh sensitivity in a fair manner, the same mesh is employed for RANS and LES. In steady RANS solution, flow field is the same along the spanwise x_3-direction, so a two-dimensional mesh sliced at cylinder mid-span is utilized to facilitate computational speed. In another word, mesh of 2D RANS is exactly the same as that of 3D LES in the x_1-x_2 plane.

Parameters for the three sets of mesh studied in LES are listed in Table 1. Grid size is refined in all three directions. Fig. 4 shows velocity magnitude development at centerline for each set of mesh with RANS (transition SST model) and LES. Fig. 5 contours difference of velocity magnitude between the finest and coarsest meshes in RANS and LES. One common observation from these two figures is velocity change with different mesh resolution is much stronger in LES than in RANS. Velocity difference between the finest and coarsest mesh is obviously higher in LES, and spreads over a wider area all along the buoyant plume, as shown in Fig. 5. For velocity value at centerline, the maximum difference between the finest and coarsest mesh is 15% in LES, while it decreases to 10% in RANS, according to Fig. 4. This demonstrates LES is more sensitive to mesh resolution than RANS, resonating the proposition

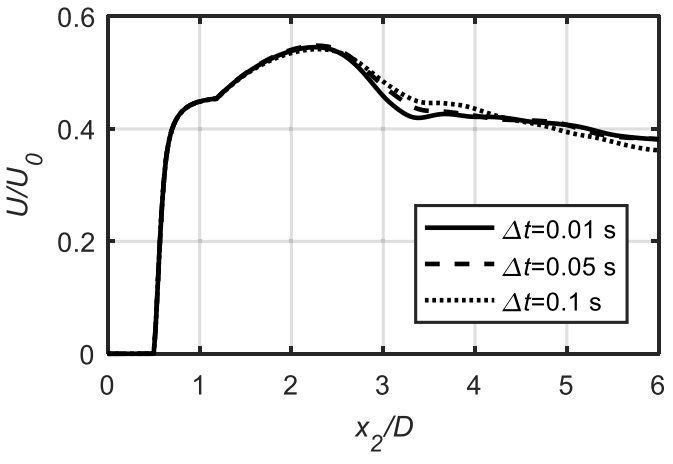

Fig. 2. Mean velocity magnitude along vertical x_2-axis at centerline ($x_1 = 0$ mm) for three time steps.

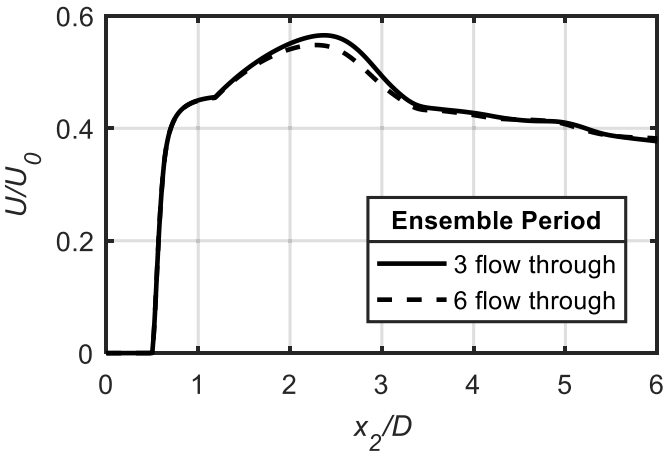

Fig. 3. Mean velocity magnitude along vertical x_2-axis at centerline ($x_1 = 0$ mm) for two ensemble-averaging time periods in LES.

by He and Yi [50] and Léonard et al. [47].

Fig. 4 also provides evidence of mesh adequacy. Velocity magnitude shows a converging trend as the mesh is refined. The maximum velocity difference shrinks from above 10% between the coarsest and intermediate mesh to within 5% between the intermediate and finest mesh. Thus, the intermediate mesh is adequate for LES and RANS, which has a grid size of 6,250,000 and 125,000 respectively.

2.2.4. Sensitivity to boundary condition settings

On the two lateral sides of the computational domain shown in Fig. 1, boundary condition of static pressure is specified originally. For the purpose of comparison, periodic boundary condition is also designated to these two sides, which is used in the LES computation by Grafsrønningen and Jensen [51]. Intuitively speaking, the choice between these two boundary condition settings should have little impact on the simulation results in buoyant plume, because the domain has a sufficiently large width of 20D.

However, this is true only for RANS rather than LES, as demonstrated in Fig. 6, which shows the effect of the two boundary condition settings on the centerline velocity along vertical x_2-axis. It is clearly seen that LES is far more sensitive to boundary condition setup than RANS. Maximum difference of velocity magnitude between using periodic and pressure outlet boundary conditions reaches 27% for LES (at x_2/D = 3.3), however, it stays within 1.5% for RANS.

To sum up, LES is notably less robust to mesh inadequacy and the choice of boundary conditions, as verified by numerical tests in this section. Ramification of boundary condition setting on simulation veracity with respect to experimental data will be discussed in next section.

2.3. Validation

2.3.1. Heat transfer on cylinder surface

Nusselt number along the circumference of cylinder surface is shown in Fig. 7 and compared with experimental data obtained from tube temperature measurements by Grafsrønningen et al. [11]. The common qualitative trend among experimental data, LES and six RANS models is the same. Nusselt number keeps declining from the stagnation point at the bottom to trailing edge at the top, indicating no transition to turbulence occurs on the cylinder and the flow stays laminar. Hence, surface heat transfer is not sensitive to turbulence models. CFD results with various models collapse to a single curve. The quantitative difference between experiment and CFD is within 10% for most part of the cylinder except near trailing edge (θ = [160°, 180°]), where thermal boundary layer separates and merges into buoyant plume, according to Kuehner et al. [15]. In this region, relatively large deviation between experiment

Table 1
Parameters of mesh independence study (LES).

Grid size	Nodes on cylinder	Min grid size near wall[mm]	Nodes on domain depth	y^+ on cylinder	y_B^+ on cylinder
8.45 million	216	0.007	55	0.064	0.175
6.25 million	176	0.010	50	0.091	0.250
3.91 million	160	0.020	42	0.182	0.500

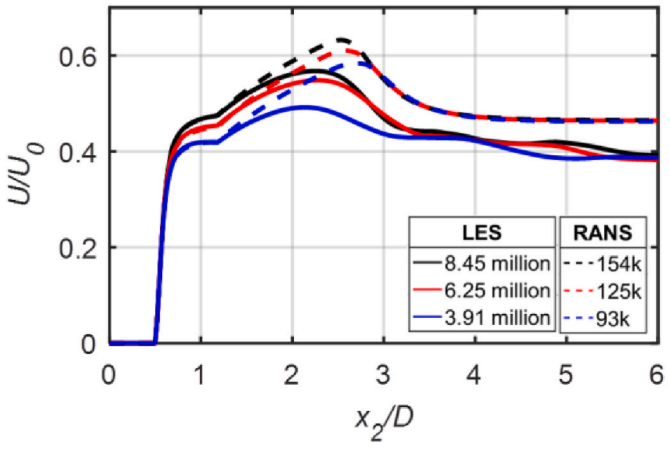

Fig. 4. Mean velocity magnitude along vertical x_2-axis at centerline ($x_1 = 0$ mm) for 3 grid sizes (mesh on x_1-x_2 plane is the same in RANS and LES).

and CFD is considered normal and has been reported in recent publications (Pelletier et al. [40]).

2.3.2. Buoyant plume velocity and its evolution

To validate the six RANS models employed, Fig. 8 displays mean velocity magnitude along horizontal x_1-axis at a vertical location of $x_2/D = 3.52$. Among all RANS models, transition SST offers the best agreement with experimental data. Maximum velocity deviation from experiment is 25%, situated at centerline ($x_1 = 0$). Plume width is also captured well. In contrast, ω-based models (k-ω SST and transition-k-kl-ω) overestimate centerline velocity by more than 60% and underestimate plume width remarkably. k-ε realizable model, k-ε RNG model and Reynolds stress model predict centerline velocity well, but plume width is off by too much. Thus, RANS with transition SST model is used in the ensuing discussions.

LES result is also validated against experimental data in Fig. 8. It shows a bit quantitative improvement in terms of matching the experiment, compared to RANS with transition SST model. Mean velocity is overpredicted by a maximum of 15% at centerline. Plume width is closer to experiment than RANS. Nevertheless, improvement in prediction accuracy by switching from RANS with transition SST model to LES is much less than that by varying RANS models. In this context, RANS with the properly selected transition SST model is a good candidate for rapid design of heat exchangers given its low computational cost. However, for the investigation of detailed flow physics, especially transitional mechanism of buoyant plume, high-fidelity LES is still necessary because its turbulence modelling approach is inherently more sensible, as discussed in Section 1.

To validate LES and RANS in simulating the development of buoyant plume more thoroughly, Fig. 9 shows the evolution of mean velocity profile at all vertical locations where experimental data are available

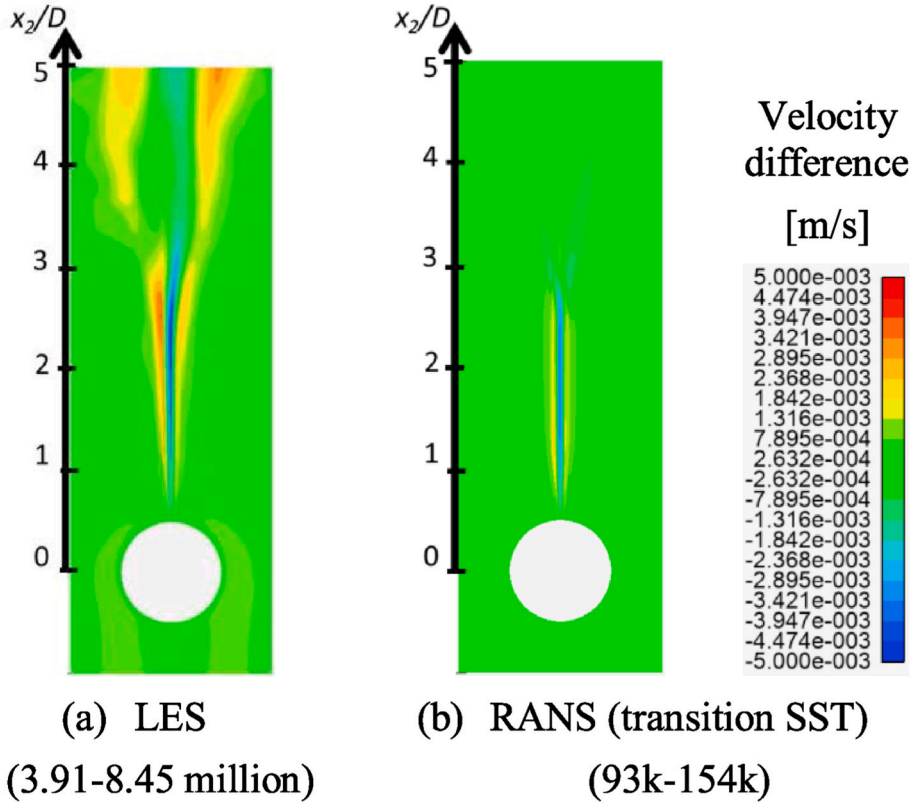

Fig. 5. Difference of velocity magnitude between the finest and coarsest meshes.

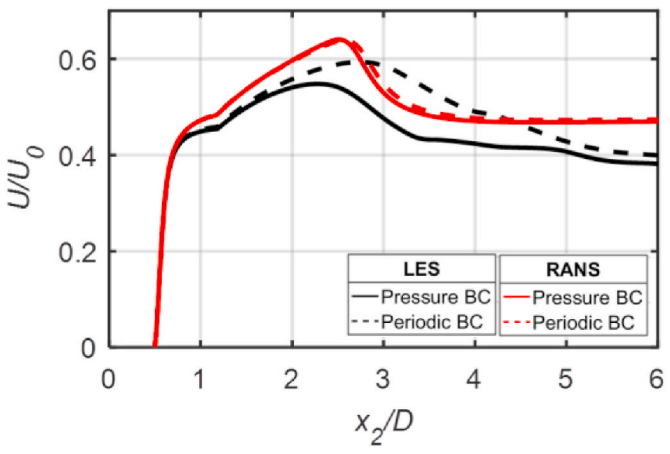

Fig. 6. Mean velocity magnitude along vertical x_2-axis at centerline ($x_1 = 0$ mm) for LES and RANS (transition SST) with pressure or periodic condition on lateral boundaries of computational domain.

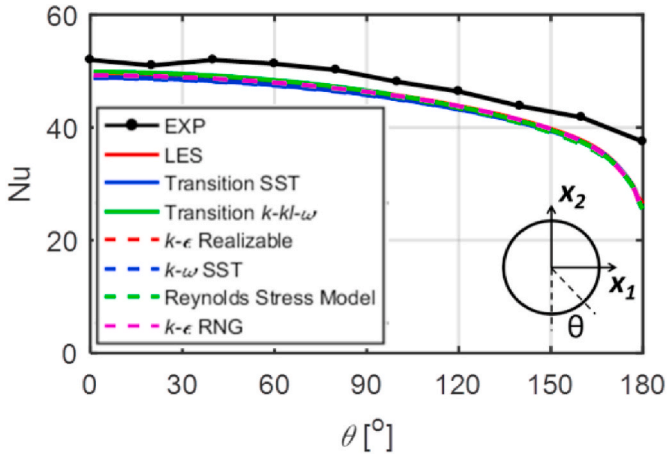

Fig. 7. Nusselt number along cylinder surface from experiment (Grafsrønningen et al. [11]), LES and 6 RANS models.

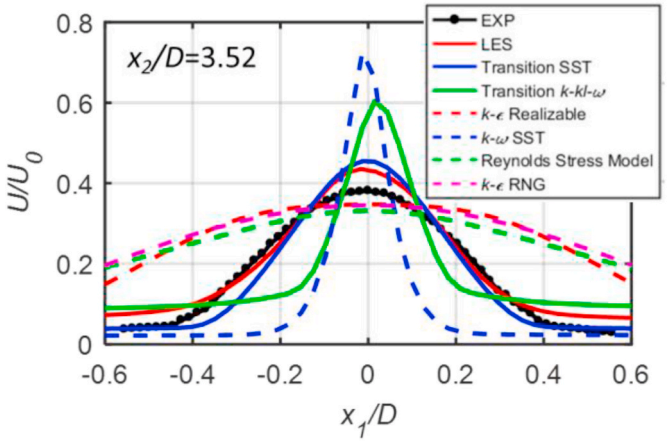

Fig. 8. Mean velocity magnitude along horizontal-$\times_1$ axis at $x_2/D = 3.52$ for experiment (Grafsrønningen et al. [11]), LES and 6 RANS models.

(Grafsrønningen et al. [11]). Three major conclusions can be drawn from this informative figure.

Firstly, compared to pressure condition on lateral boundaries, periodic boundary condition in LES clearly generates a narrower plume with higher centerline velocity, especially after 2.78D downstream cylinder center, while that in RANS makes no difference, which is in concert with the conclusion in Section 2.2.4. Furthermore, its results deviate further away from experimental data compared to pressure boundary condition in LES, and become even worse than RANS. For instance, when switching from pressure to periodic boundary condition at $x_2/D = 3.15$, the overprediction in centerline velocity for LES increases from 20% to 53%, while that for RANS stays at 32%. Underprediction in plume width becomes more intense for LES and exceeds that for RANS. In fact, fluid is drawn into the computational domain across lateral boundaries due to buoyant effect of thermal plume, although at a small velocity when the domain width gets very large. So periodic boundary condition is not physically accurate, and this error is amplified greatly in LES. Therefore, using periodic boundary condition in LES for natural convection around unconfined horizontal cylinders should be alarmed.

Secondly, validation of LES with pressure condition on lateral boundaries against experimental data shows satisfactory agreement in general. Velocity magnitude at centerline has a minimum error of 15% at $x_2/D = 3.52$ and a maximum error of 48% at $x_2/D = 1.67$. Plume width is computed reasonably well except at $x_2/D = 2.41$ and 2.78. Performance of current LES is justified when gauging against the preceding study by Grafsrønningen and Jensen [51] at a similar Rayleigh number. In their LES computation, centerline mean velocity deviates from experimental data by a minimum of 52% and a maximum of 143% in a similar range of locations, which is almost three times larger than the present study. Moreover, their computational domain has a width of 75D and a height of 150D, which is 18 times bigger than the current CFD. Therefore, the present LES computation remarkably improves accuracy and speed in the state of the art. This is partly attributed to specifying pressure condition on the lateral boundaries of domain, which is more physically sensible than periodic boundary condition and could reduce the overprediction in centerline velocity remarkably, as described before.

Lastly, comparison between RANS and LES with pressure condition on lateral boundaries in Fig. 9 shows they follow the same qualitative trend with experiment. In quantitative sense, RANS accuracy is inferior to LES only marginally. Velocity magnitude at centerline has a minimum error of 32% and a maximum error of 65% for RANS, which is about 15% higher than that of LES. Plume width predicted by RANS is almost the same as LES. In the context that error caused by varying RANS models can easily reach 60% as shown in Fig. 8, it is suggested that heat exchanger designers use the properly-selected RANS model (transition SST) to achieve an accuracy that is comparable to LES at a much lower computational cost. But for physical investigation of buoyant plume transitional mechanism, which is the focus of the present research, finely-tuned LES (with pressure condition on lateral boundaries of computational domain) is required and will be used in the remaining part of this paper.

One minor observation from Fig. 9 is the velocity magnitude far away from the cylinder tends to be overpredicted by 1–2 mm/s, especially for LES. This is probably caused by the error of using pressure inlet and outlet boundary condition on the top and bottom of computational domain, which generates upward through-flow even far from the cylinder. In experiment, water is bounded by walls and free surface in a large tank, as depicted by Grafsrønningen et al. [11]. CFD with adiabatic wall and free water surface on the bottom and top boundary respectively was also implemented, but the large scale vortices forming beneath free surface would disrupt the weak buoyant plume tremendously, similar to the situation reported by Grafsrønningen and Jensen [51]. Since the focus of this paper is buoyant plume which resides around the central area, the slight discrepancy in the far-field can be neglected.

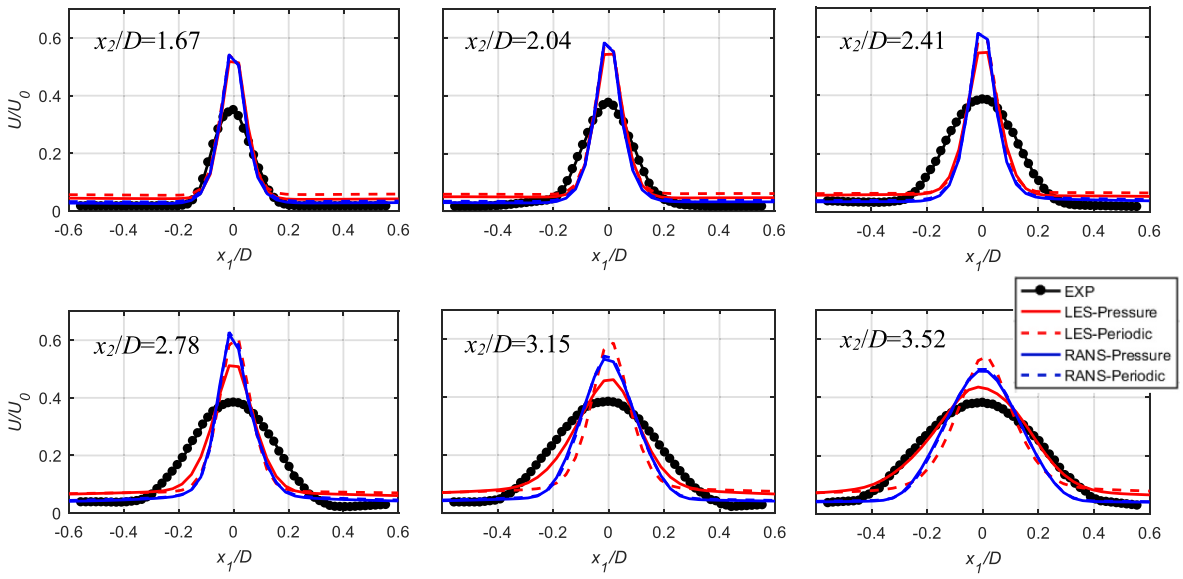

Fig. 9. Mean velocity magnitude along horizontal x_1-axis at six vertical locations from experiment (Grafsrønningen et al. [11]), LES and RANS (transition SST) with pressure and periodic condition on lateral boundaries.

3. Results and analyses

3.1. Mean flow

Mean velocity magnitude from LES and RANS with transition SST model is contoured in Fig. 10. LES and RANS results exhibit similar qualitative pattern. They consistently show that thermal plume accelerates after leaving the heated cylinder until $x_2/D = 2.3$ and then decelerates while becoming more dispersive transversely, indicating enhanced dissipation level. This phenomenon is further substantiated in Fig. 11, which shows mean velocity magnitude at the plume centerline. Plume acceleration after leaving the heated cylinder can also be observed in the PIV data (Kuehner et al. [14,15]), RANS (Kumar et al. [25]) and LES results (Devenish et al. [60]), but has not been explicitly discussed and analyzed in these literature.

Fig. 10 also shows that plume width in LES is a little bigger than RANS after $x_2/D = 2.3$, and velocity near plume center is smaller than RANS. This suggests that RANS generates a thermal plume whose velocity profile is more centralized, echoing the observation in Fig. 9.

Mean temperature difference ($\overline{\Delta T} = \overline{T} - T_\infty$) results from LES and RANS are contoured in Fig. 12, non-dimensionalized by the value at a circumferential angle of 90°. Temperature contour shows the same qualitative trend with interferometry measurement data by Narayan et al. [61], although their medium is air. Both LES and RANS

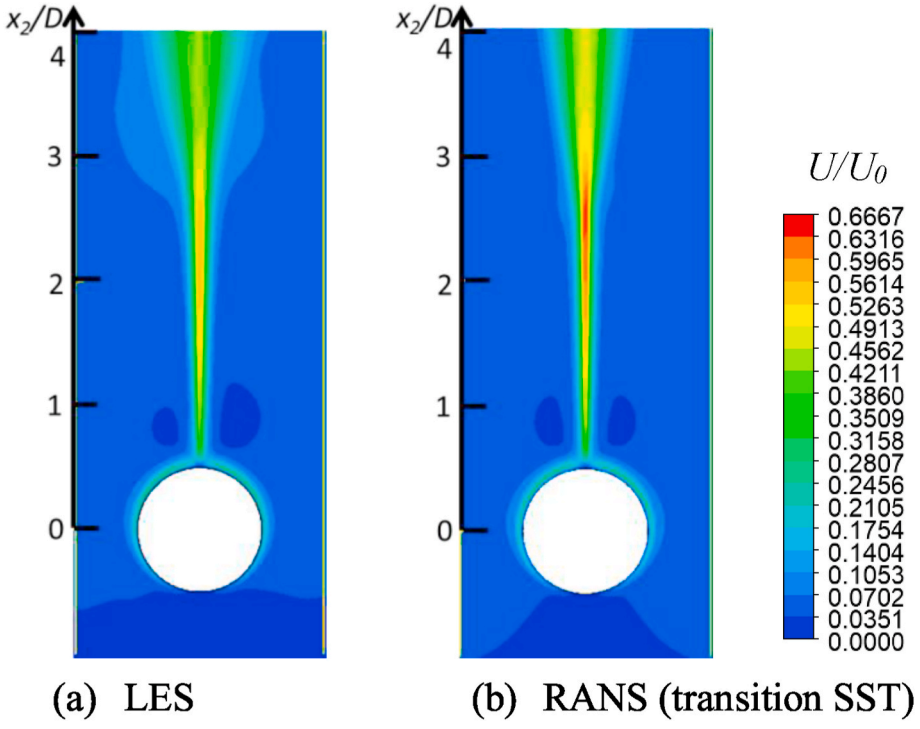

Fig. 10. Mean velocity magnitude.

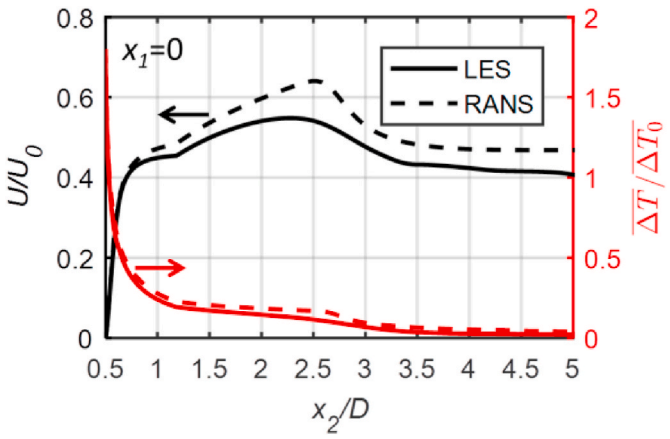

Fig. 11. Dimensionless mean velocity magnitude and mean temperature difference at plume centerline ($\times_1 = 0$).

consistently illustrate that temperature decreases as buoyant plume rises, due to heat dissipation into atmosphere. Temperature decrease along the plume centerline is also shown explicitly in Fig. 11. From the first law of thermodynamics, plume acceleration right after the cylinder must be attributed to work input, which is confirmed in the contour of mean total gauge pressure in Fig. 13. It follows the same qualitative trend as mean upward velocity. Mean total pressure increases downstream of the cylinder until $x_2/D = 2.3$, indicating work input from buoyancy force which contributes to augmentation of mean kinetic energy and thus, mean velocity, as demonstrated in Fig. 10. Detailed mechanism of buoyancy work will be discussed further in Section 3.3.

3.2. Turbulence properties

To explore detailed physics of transitional buoyant plume, the finely-tuned LES results with pressure condition on lateral boundaries are analyzed in the following. Velocity, temperature and pressure is decomposed into mean and fluctuating components as,

$$u_i = U_i + u_i' \tag{21}$$

$$\Delta T = \overline{\Delta T} + T' \tag{22}$$

$$p = P + p' \tag{23}$$

Fig. 14 contours turbulent kinetic energy, which is defined as $k = (\overline{u_1'^2} + \overline{u_2'^2} + \overline{u_3'^2})/2$, and fluctuating velocity components ($\overline{u_1'^2}$, $\overline{u_2'^2}$), non-dimensionalized by $1/U_0^2$. Velocity fluctuation first appears in the vertical component ($\overline{u_2'^2}$) and rises gradually to reach the maximum, where thermal plume and begins to sway horizontally, manifested by the appearance of horizontal velocity fluctuation ($\overline{u_1'^2}$). Turbulent kinetic energy generally follows the same qualitative pattern as upward velocity fluctuation ($\overline{u_2'^2}$).

To study thermal plume development quantitatively, a horizontal line cut is created in the heated plume, which is represented by an iso-volume of $\overline{\Delta T} \geq 0.05K$ at $x_3 = 2D$ (mid-span), and the transversely averaged dimensionless turbulent kinetic energy and fluctuating velocity components is plotted against the streamwise coordinate in Fig. 15. Flow unsteadiness originates in vertical velocity at $x_2/D = 1$. Vertical velocity fluctuation grows gradually to reach the maximum at $x_2/D = 2.8$. Plume begins to sway at $x_2/D = 2.3$, manifested by the initiation of horizontal velocity fluctuation. The swaying motion is climaxed at $x_2/D = 3.8$ and then dwindles.

Transversely averaged turbulent kinetic energy starts to grow at $x_2/D = 1$, indicating the onset of transition to turbulence. It keeps increasing until $x_2/D = 3.8$ and then decreases to approach an asymptotic value, which indicates that transition ends and the flow enters fully-developed turbulent regime, according to the criterion stated by Elicer-Cortes et al. [19]. Thus, transition to turbulence begins at $Gr_{x2} = 1.5 \times 10^8$ and ends at $Gr_{x2} = 7 \times 10^9$, where streamwise Grashof number $Gr_{x2} = g\beta(T_w - T_\infty)x_2^3/v^2$. This result falls within the range predicted through the transition criteria proposed by Noto et al. [17] and Bill and Gebhart [62].

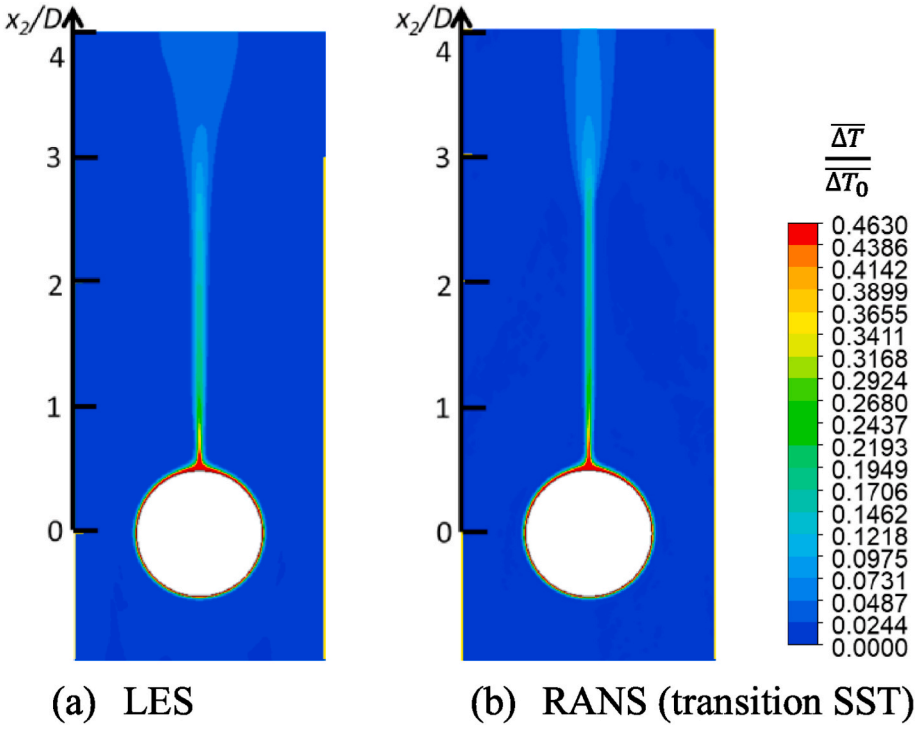

Fig. 12. Mean temperature difference.

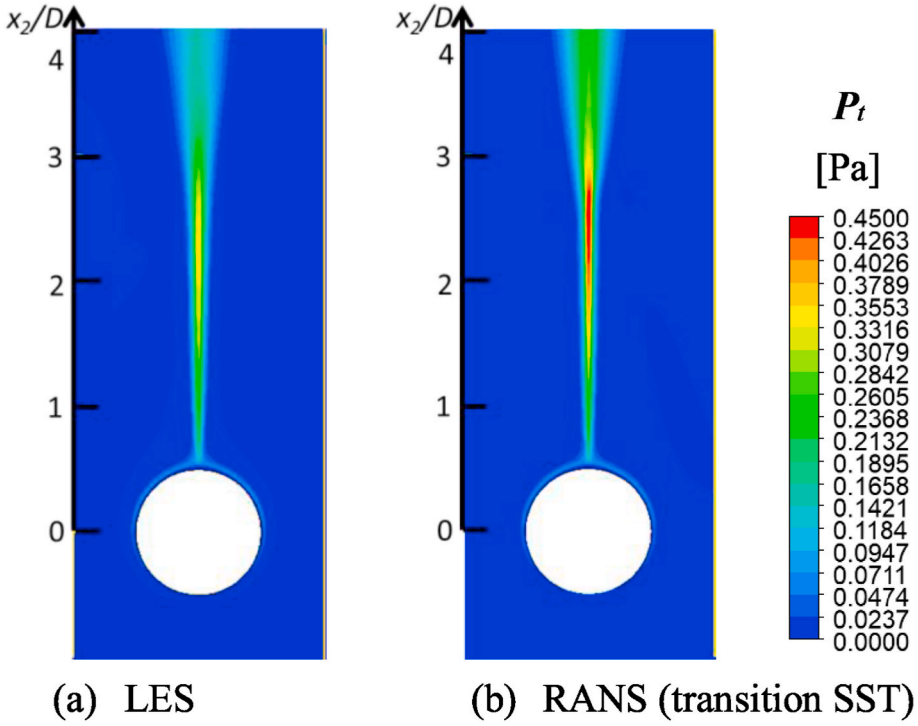

Fig. 13. Mean total gauge pressure.

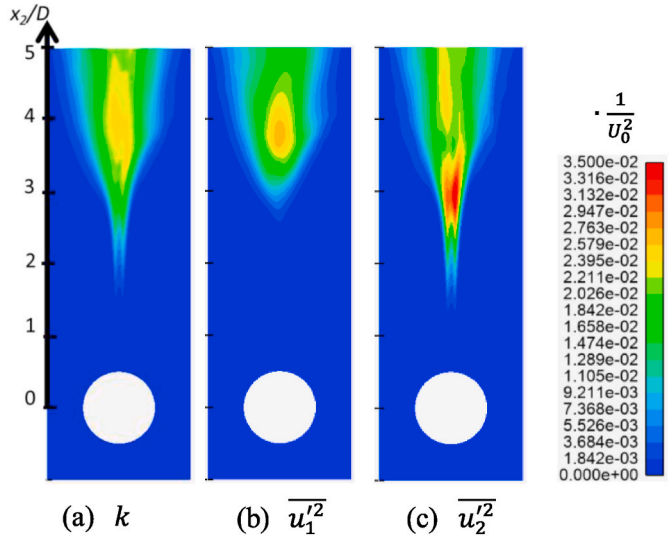

Fig. 14. Turbulent kinetic energy (k) and fluctuating velocity components ($u_1^{'}$, $u_2^{'}$), non-dimensionalized by.$1/U_0^2$

Power spectral density of temperature for a centerline point at $x_2/D = 3.9$ is illustrated in Fig. 16, which is obtained from LES result with a time step of 0.01 s and ensemble-averaging period of 100 s. The graph shows the same qualitative trend as a preceding LES study on natural convection in a horizontal annular cavity (Padilla and Silveira-Neto [63]). Power spectral density at frequencies bigger than 5 Hz collapses nicely to a slope of −5/3, reflecting the inertial subrange of turbulence as predicted by Kolmogorov hypothesis. Hence the flow has become fully turbulent here, as expected from previous analysis. Besides, the inertial subrange starts from a frequency of 5 Hz (time period of 0.2 s). Hence, time step size in LES must be lower than 0.2 s to fall in the inertial subrange and legitimize subgrid-scale turbulence modelling, which reaffirms our choice of time step size depicted in Section 2.2.1.

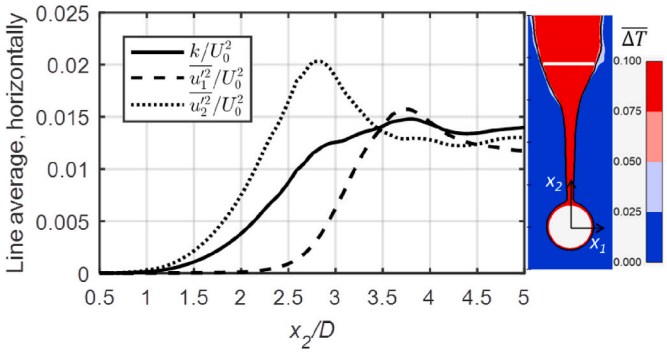

Fig. 15. Average dimensionless turbulent kinetic energy (k) and fluctuating velocity components ($u_1^{'}$, $u_2^{'}$) on a horizontal line cut within heated plume ($\overline{\Delta T} \geq 0.05K$).

3.3. Budget of kinetic energy

The equation of mean motion for thermal plume with Boussinesq approximation, as presented by Tennekes and Lumley [64], is

$$U_j\frac{\partial U_i}{\partial x_j}+\frac{\partial}{\partial x_j}\overline{u_i^{'}u_j^{'}}=-\frac{1}{\rho}\frac{\partial P}{\partial x_j}+\nu\frac{\partial^2 U_i}{\partial x_i\partial x_j}+\frac{g}{T_0}\overline{\Delta T}\delta_{i2} \tag{24}$$

Energy equation of mean flow for buoyant plume with Boussinesq approximation can then be obtained by multiplying equation (24) with U_i as

$$U_j\frac{\partial}{\partial x_j}\left(\frac{1}{2}U_iU_i\right)=\frac{\partial}{\partial x_j}\left(-\frac{P}{\rho}U_j+2\nu U_iS_{ij}-\overline{u_i^{'}u_j^{'}}U_i\right)-2\nu S_{ij}S_{ij}+\overline{u_i^{'}u_j^{'}}S_{ij}$$
$$+g\beta\overline{\Delta T}U_i\delta_{i2} \tag{25}$$

where the mean shear strain rate $S_{ij}=\frac{1}{2}\left(\frac{\partial U_i}{\partial x_j}+\frac{\partial U_j}{\partial x_i}\right)$. The above equation for mean kinetic energy ($K=U^2/2$) has three source terms: rate of work done by buoyancy force ($W_{buoy}^{\cdot}=g\beta\overline{\Delta T}U_i\delta_{i2}$), rate of viscous

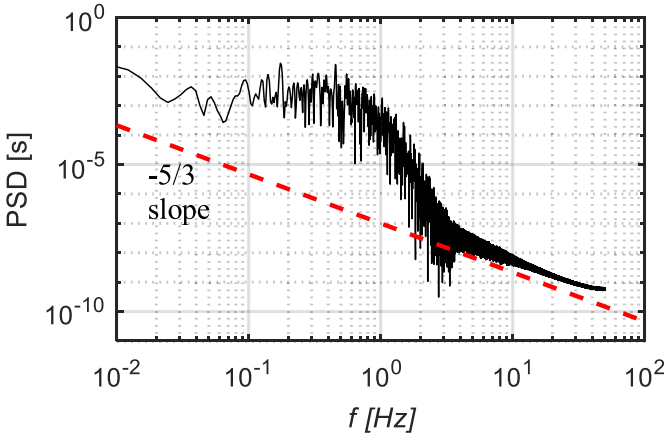

Fig. 16. Power spectral density of temperature for a point at (x_1, x_2, x_3)=(0, 3.9D, 2D), from LES result with a time step of 0.01 s and ensemble-averaging period of 100 s (dashed red line has a slope of −5/3).

dissipation ($\dot{\varepsilon_{vis}} = -2\nu S_{ij}S_{ij}$) and rate of turbulence dissipation, or deformation work done by turbulent stresses which transfers energy from mean flow to turbulence ($\dot{\varepsilon_{turb}} = \overline{u_i'u_j'}S_{ij}$). The net source ($\dot{S} = \dot{W_{buoy}} + \dot{\varepsilon_{vis}} + \dot{\varepsilon_{turb}}$) contributes to the net change in mean kinetic energy, while the spatial transport terms only redistribute energy within a control volume, according to the Gauss theorem.

Turbulent energy budget, which governs kinetic energy of turbulent velocity fluctuations ($\frac{1}{2}\overline{u_i'u_i'}$), is also presented by Tennekes and Lumley [64] as

$$U_j\frac{\partial}{\partial x_j}\left(\frac{1}{2}\overline{u_i'u_i'}\right) = -\frac{\partial}{\partial x_j}\left(\frac{1}{\rho}\overline{u_j'p'} + \frac{1}{2}\overline{u_i'u_i'u_j'} - 2\nu\overline{u_i's_{ij}}\right) - \overline{u_i'u_j'}S_{ij} - 2\nu\overline{s_{ij}s_{ij}} \quad (26)$$

For thermal plume with Boussinesq approximation, turbulent energy budget is derived from equation (26) by adding a source term related to buoyancy as

$$U_j\frac{\partial}{\partial x_j}\left(\frac{1}{2}\overline{u_i'u_i'}\right) = -\frac{\partial}{\partial x_j}\left(\frac{1}{\rho}\overline{u_j'p'} + \frac{1}{2}\overline{u_i'u_i'u_j'} - 2\nu\overline{u_i's_{ij}}\right) - \overline{u_i'u_j'}S_{ij} - 2\nu\overline{s_{ij}s_{ij}} + g\beta\overline{T'u_i'}\delta_{i2} \quad (27)$$

where $s_{ij} = \frac{1}{2}\left(\frac{\partial u_i'}{\partial x_j} + \frac{\partial u_j'}{\partial x_i}\right)$. This equation has three source terms: turbulence production rate by buoyancy ($\dot{G_k} = g\beta\overline{T'u_i'}\delta_{i2}$), viscous dissipation rate in turbulence ($\varepsilon = -2\nu\overline{s_{ij}s_{ij}}$), and turbulence production rate by mean shear ($\dot{P_k} = -\overline{u_i'u_j'}S_{ij}$), which exchanges energy between mean flow and turbulence and is the negative of turbulence dissipation rate ($\dot{\varepsilon_{turb}}$) in the equation of mean flow kinetic energy.

In this section, energy budget for mean flow and turbulence is analyzed based on LES results. From dimensional analysis, source terms in equations of mean flow and turbulence should be on the same order of magnitude as $D^2/\nu U_0^2$, so they are non-dimensionalized by $D^2/\nu U_0^2$ in subsequent discussions.

3.3.1. Mean flow

Source terms in the equation of mean kinetic energy are contoured in Fig. 17. Buoyancy force exerts positive work on thermal plume, contributing to increase of mean kinetic energy. It is the largest at the trailing edge of cylinder and reduces as buoyant plume rises, indicating the decay of mean temperature is faster than the amplification of mean upward velocity. Dissipation of mean kinetic energy occurs on the outer edge of buoyant plume, where the mean shear is the largest. Viscous dissipation resides at $x_2/D < 2.5$ and is much lower than turbulence dissipation, which is mainly located at $x_2/D = [2,4]$. Net source of these three terms basically follows the distribution of buoyancy work, except

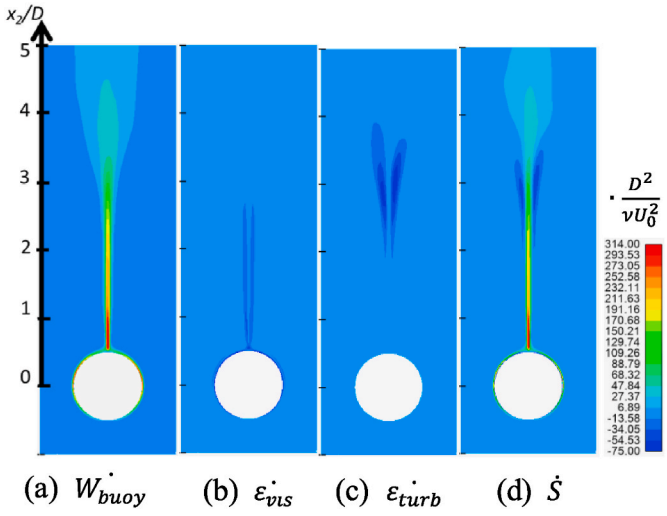

Fig. 17. Rate of buoyancy work ($\dot{W_{buoy}}$), viscous dissipation ($\dot{\varepsilon_{vis}}$), turbulence dissipation ($\dot{\varepsilon_{turb}}$) and net source ($\dot{S}$) in mean kinetic energy equation, non-dimensionalized by $D^2/\nu U_0^2$

on the outer edge of thermal plume at $x_2/D = [2,4]$ where dissipation into turbulence is eminent. This indicates buoyancy work dominates among the source terms and thus, the change of mean kinetic energy in most parts of thermal plume.

Quantitative comparison of buoyancy work, viscous and turbulence dissipation is presented in Fig. 18, which shows the work rates integrated on a horizontal line cut in heated plume whose $\overline{\Delta T} \geq 0.05K$ at $x_3 = 2D$ (mid-span), plotted against the vertical coordinate. Compared to buoyancy work, viscous dissipation is very small and only manifests within 2.5D downstream cylinder center. Turbulence dissipation, which transfers energy from mean flow to turbulence, initiates at $x_2/D = 1$ and grows gradually to exceed viscous dissipation at $x_2/D = 2.3$. It then increases rapidly to reach the maximum value at $x_2/D = 3.1$ and dwindles after that. Hence, thermal plume is laminar until $x_2/D = 1$ and then transits to turbulence, which agrees with the conclusion in Section 3.2. Overall speaking, buoyancy work prevails over dissipation into turbulence and molecular viscosity except in a small region near $x_2/D = 3.1$, where turbulence dissipation is maximum and the net source is negative.

Mean kinetic energy integrated on a horizontal line cut in heated

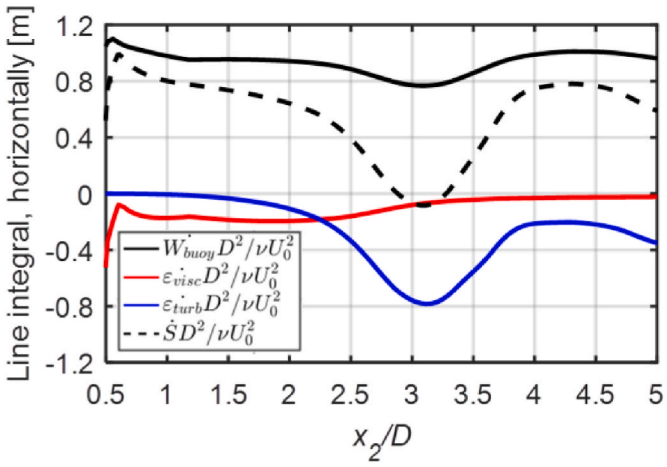

Fig. 18. Rate of dimensionless buoyancy work ($\dot{W_{buoy}}$), viscous dissipation ($\dot{\varepsilon_{vis}}$), turbulence dissipation ($\dot{\varepsilon_{turb}}$) and net source ($\dot{S}$) in mean kinetic energy equation, integrated over a horizontal line cut within heated plume ($\overline{\Delta T} \geq 0.05K$).

plume whose $\overline{\Delta T} \geq 0.05K$ is plotted against the streamwise coordinate in Fig. 19. As thermal plume develops, integral mean kinetic energy keeps increasing because horizontally-integrated net source is mostly positive, which is dominated by the input of buoyancy work as depicted before. Fig. 19 also presents the streamwise variation of averaged mean kinetic energy on the same horizontal line cut. It is observed that transversely-averaged mean kinetic energy rises before $x_2/D = 2.3$, because energy dissipation mainly comes from molecular viscosity, which is very small compared to the predominant buoyancy work. It then reduces because turbulence dissipation becomes the major loss mechanism and increases rapidly, leading to enhanced cross-stream diffusivity and thus, smoothing of transverse velocity distribution. Finally, it is stabilized after $x_2/D = 3.8$ where thermal plume enters fully-turbulent regime.

Smoothing of transverse distribution of dimensionless mean kinetic is demonstrated in Fig. 20. Before 2D downstream cylinder center, both peak value and width of thermal plume increases because plume accelerates and enlarges subject to the dominant buoyancy work. After 2D downstream cylinder center, plume continues to widen, but the peak value plateaus or decreases, leading to the reduction of transversely-averaged mean kinetic energy as shown in Fig. 19. Again, this is caused by the augmentation in turbulence dissipation, which is much more diffusive than viscous dissipation. Smoothing of transverse velocity distribution is also presented in PIV measurement data of Grafsrønningen et al. [11] and Grafsrønningen and Jensen [12]for transitional buoyant plume.

3.3.2. Turbulence

Production rate of turbulent kinetic energy by buoyancy and mean shear is illustrated in Fig. 21. Overall speaking, turbulence production by mean shear is larger than that by buoyancy. So the total turbulence production ($\dot{P}_k + \dot{G}_k$) follows the same qualitative trend as turbulence production by mean shear. In addition, generation of turbulence initiates at certain distance downstream the cylinder. Production by buoyancy is situated in central region of the plume, while that by mean shear is located on the outer edge of the plume. Moreover, from the definition of $\dot{G}_k$, $\overline{T'u_2} > 0$ in thermal plume, indicating temperature and upward velocity is positively correlated, forming an unstable atmosphere according to Tennekes and Lumley [64].

Quantitative comparison of turbulence production by buoyancy, mean shear and their summation is presented in Fig. 22, which shows the production rates integrated on a horizontal line cut in heated plume whose $\overline{\Delta T} \geq 0.05K$, plotted against the vertical coordinate. Again, turbulence production by mean shear is greater than that by buoyancy. In another word, generation of turbulent kinetic energy mostly comes from mean shear rather than buoyancy. Buoyancy enters the kinetic energy budget mainly from mean flow, instead of turbulence. This is in concert

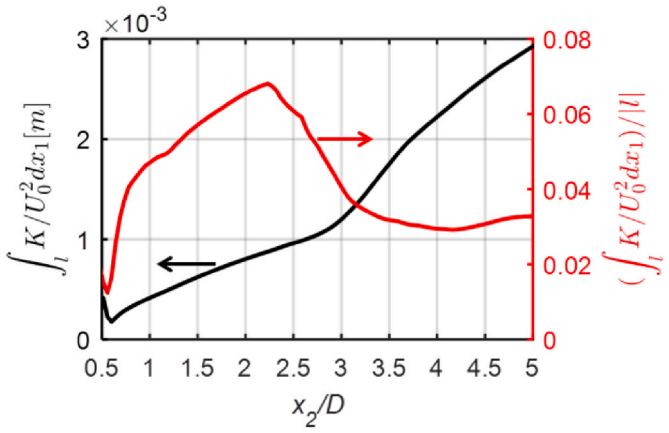

Fig. 19. Integral dimensionless mean kinetic energy (K/U_0^2) on a horizontal line cut within heated plume ($\overline{\Delta T} \geq 0.05K$), as well as the line-averaged value.

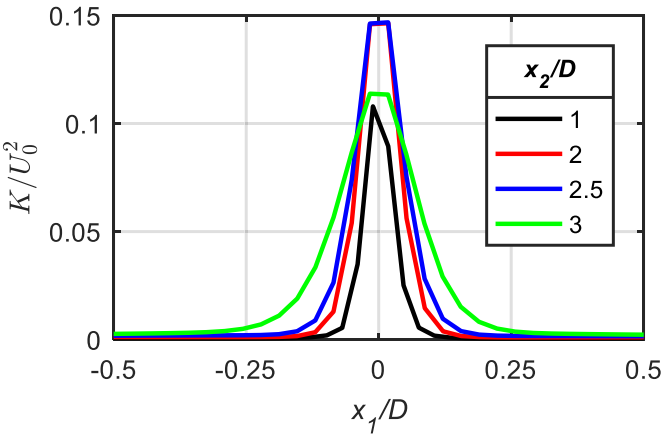

Fig. 20. Transverse distribution of dimensionless mean kinetic energy at different steamwise locations.

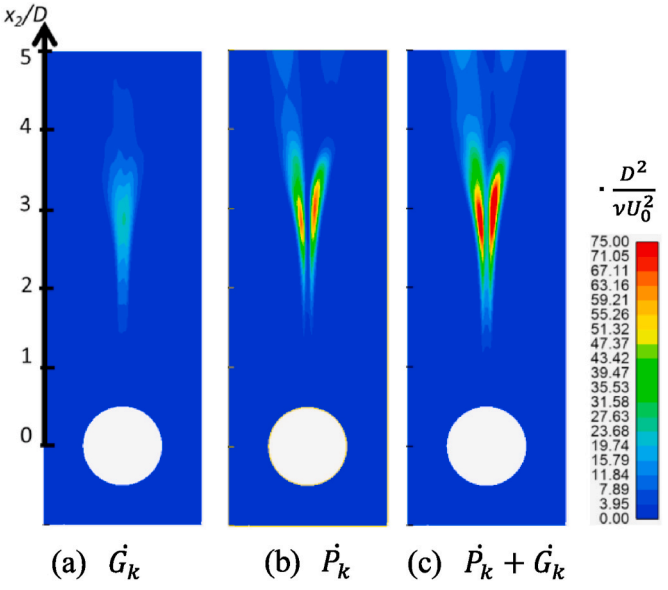

Fig. 21. Turbulence production rate by buoyancy ($\dot{G}_k$) and mean shear ($\dot{P}_k$), non-dimensionalized by $D^2/\nu U_0^2$

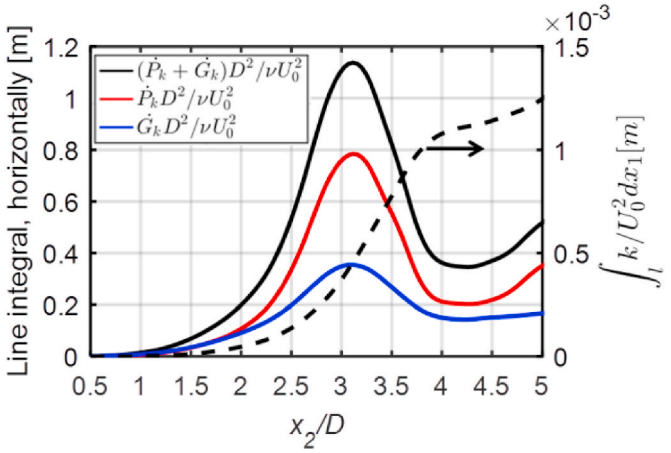

Fig. 22. Dimensionless turbulence production rate by buoyancy ($\dot{G}_k$) and mean shear ($\dot{P}_k$), as well as turbulent kinetic energy (k), integrated over a horizontal line cut within heated plume ($\overline{\Delta T} \geq 0.05K$).

with the findings by Grafsrønningen and Jensen [12] and Shabbir and George [65].

Fig. 22 also displays streamwise variation of turbulent kinetic energy integrated on the horizontal line cut. Turbulent kinetic energy departs from zero as early as $x_2/D = 1$, where turbulence production by buoyancy and mean shear begins to grow and thermal plume begins transitioning to turbulence. Integral turbulent kinetic energy keeps increasing downstream, indicating total turbulence production outweighs viscous dissipation in turbulence. The sharpest rise in turbulent kinetic energy occurs at $x_2/D = 3.1$, where integral turbulence production rate is maximum.

Up to this point, transition mechanism of buoyant plume has been elucidated. Plume is laminar and accelerates after leaving the heated cylinder, due to work done by buoyancy force. Flow unsteadiness appears first in upward velocity at $x_2/D = 1$ ($Gr_{x2} = 1.5 \times 10^8$), where turbulence production by buoyancy and mean shear initiates and thermal plume starts transitioning to turbulence. Plume continues to accelerate until it begins to sway horizontally at $x_2/D = 2.3$ (near the middle of transitional regime), where energy dissipation from mean flow to turbulence becomes the driving loss mechanism, overriding that by molecular viscosity. Consequently, plume becomes much more diffusive and thus, transverse velocity distribution is smoothened. Afterward turbulence dissipation increases quickly and thus, transversely-averaged mean kinetic energy reduces. Transversely-averaged turbulent kinetic energy keeps increasing upon its initiation at $x_2/D = 1$ until $x_2/D = 3.8$ ($Gr_{x2} = 7 \times 10^9$) where plume swaying is climaxed. It then reduces to approach an asymptotic value, indicating that transition ends and plume enters fully-developed turbulence regime.

4. Conclusions

This paper presents the first of the kind LES study with acceptable accuracy as compared to the state of the art for natural convection heat transfer and fluid flow around a single horizontal cylinder, based on which new physical insight about the laminar-to-turbulent transition of buoyant plume is elucidated. A well-calibrated LES study was conducted for a single horizontal cylinder in water at a Rayleigh number of 8×10^7, complemented by RANS computations for comparison purposes. Numerical sensitivity to time step size, ensemble-averaging period, mesh resolution and boundary condition is thoroughly tested. Simulation results are then validated in terms of Nusselt number on cylinder surface and buoyant plume velocities at six streamwise locations, by comparing with the experimental data of Grafsrønningen et al. [11] whenever possible.

It is discovered that LES is far more sensitive to numerical settings of grid resolution and boundary condition than RANS. In particular, an alarm is set for using periodic condition in LES on lateral boundaries of computational domain, because it makes the predicting error enlarge by up to 30% compared to the more realistic pressure condition, and even exceed that of RANS. LES with pressure condition on lateral boundaries shows acceptable accuracy compared to experimental data. Simulation error of centerline velocity is in the range of 15%–48%, which is only one third of the level reported by Grafsrønningen and Jensen [51] who uses periodic boundary condition.

Next, the finely-tuned and well-calibrated LES results are analyzed to reveal the physical mechanism that governs buoyant plume evolution from the single horizontal cylinder, with an emphasis on the transitional regime, through investigating the mean flow and turbulence characteristics, as well as the associated budget in kinetic energy.

Transition from laminar to turbulence onsets at a streamwise Grashof number of 1.5×10^8 ($x_2/D = 1$), manifested by the initiation of vertical velocity fluctuation and turbulent kinetic energy. Transversely-averaged turbulent kinetic energy keeps increasing until the streamwise Grashof number reaches 7×10^9 ($x_2/D = 3.8$) where horizontal velocity fluctuation reaches maximum. It then reduces to approach an asymptotic value, signifying the end of transition. Afterward, buoyant plume enters fully-developed turbulent state.

New physical insights about buoyant plume evolution are presented. After leaving the heated cylinder, buoyant plume accelerates while its temperature keeps decreasing due to heat loss to the atmosphere. This is because buoyancy force exerts work on thermal plume, contributing to increase of mean kinetic energy and thus, plume acceleration. In this region, buoyant plume is laminar or at the initial stage of transition. So the loss of mean kinetic energy mainly comes from molecular viscosity, which is much smaller than the generation of mean kinetic energy from work done by buoyancy force. The plume continues to accelerate until it begins to sway at 2.3 diameters downstream cylinder center, which is near the middle of transitional regime. Thereafter, energy dissipation from mean flow to turbulence increases quickly to become the major loss mechanism, overriding that by molecular viscosity. As a result, diffusivity of thermal plume is augmented notably due to turbulent stresses, leading to the smoothing of transverse mean velocity distribution. Transversely-averaged mean kinetic energy reduces and finally stabilizes after thermal plume enters fully-turbulent regime ($x_2/D \geq 3.8$). Overall speaking, buoyancy work prevails over energy dissipation into turbulence and molecular viscosity, leading to monotonic increase of transversely-integrated mean kinetic energy along the streamwise direction of thermal plume. Production of turbulent kinetic energy, however, mainly comes from mean shear rather than buoyancy.

Declaration of competing interest

The authors declare that they have no known competing financial interests or personal relationships that could have appeared to influence the work reported in this paper.

Data availability

Data will be made available on request.

Acknowledgements

The authors would like to thank the financial support from EPSRC Global Challenges Research Fund (EP/P028829/1). Prof. Zhibin Yu and Dr. Guopeng Yu in University of Glasgow, as well as Dr. Sham Rane in University of Oxford are also acknowledged for their inputs and valuable discussions.

Nomenclature

Symbols

D	Diameter of cylinder [m]
f	Frequency [Hz]
Gr	Grashof number ($= g\beta(T_w - T_\infty)D^3/\upsilon^2$)
Gr_{x2}	Streamwise Grashof number ($= g\beta(T_w - T_\infty)x_2^3/\upsilon^2$)
g	Gravitational acceleration [m/s^2]
K	Mean kinetic energy [m^2/s^2] ($= U^2/2$)

Nu	Nusselt number
P	Pressure [Pa]
Pr	Prandtl number
PSD	Power spectral density [s]
Ra	Rayleigh number ($=\sqrt{g\beta D^3\Delta T/(\nu\alpha)}$)
T	Temperature [K]
T_f	Film temperature [K] ($=(T_w+T_\infty)/2$)
T_w	Temperature of cylinder surface [K]
T_∞	Ambient temperature [K]
ΔT	Temperature difference [K] ($= T - T_\infty$)
$\overline{\Delta T}$	Mean temperature difference [K] ($\overline{T} - T_\infty$)
TKE, k	Turbulent kinetic energy [m^2/s^2]
t	Time [s]
Δt	Time step size [s]
U	Mean velocity magnitude [m/s]
U_0	Characteristic velocity [m/s] ($=\sqrt{g\beta D\Delta T}$)
x_1	Coordinate on horizontal axis [m]
x_2	Coordinate on vertical axis [m]
x_3	Coordinate on spanwise axis [m]
y^+	Wall distance non-dimensionalized by Kolmogorov length scale ($= n/\eta$)
y_B^+	Wall distance non-dimensionalized by conduction cut-off scale ($= n/\eta_B$)

Greek symbols

α	Thermal diffusivity [m^2/s]
β	Thermal expansion coefficient [1/K]
ε	Viscous dissipation of turbulence [m^2/s^3]
η	Kolmogorov length scale [m]
η_B	Conduction cut-off scale [m]
θ	Circumferential angle [°]
ν	Kinematic viscosity [m^2/s]
ρ	Density [kg/m^3]

Subscripts

s	static
t	total

References

[1] B.R. Gyles, B. Hægland, T.B. Dahl, A. Sanchis, S. Grafsrønningen, A. Jensen, Natural convection-subsea cooling: theory, simulations, experiments and design, in: ASME 2011 30th International Conference on Ocean, Offshore and Arctic Engineering, Rotterdam, Netherlands, 2011, pp. 11–20.

[2] H. Ma, L. He, S. Rane, Heat transfer-fluid flow interaction in natural convection around heated cylinder and its thermal chimney effect, in: International Conference on Innovative Applied Energy, Oxford, 2019.

[3] N.M. Burnside, S. Rane, G. Yu, H. Ma, N. Montcoudiol, W. Li, E.L. Teklemariam, A. Boyce, L. He, Z. Yu, Geothermally sourced combined power and freshwater generation for eastern africa. European Geothermal Congress, Den Haag, Netherlands, 2019.

[4] V.T. Morgan, The overall convective heat transfer from smooth circular cylinders. Advances in Heat Transfer, Elsevier, 1975, pp. 199–264.

[5] S.W. Churchill, H.H. Chu, Correlating equations for laminar and turbulent free convection from a horizontal cylinder, Int. J. Heat Mass Tran. 18 (9) (1975) 1049–1053.

[6] Ş.Ö. Atayılmaz, İ. Teke, Experimental and numerical study of the natural convection from a heated horizontal cylinder, Int. Commun. Heat Mass Tran. 36 (7) (2009) 731–738.

[7] G. Carlomagno, A. Cenedese, S. Iannetta, LDA velocity measurements in the buoyant plume above a heated horizontal cylinder, Arch. Mech. 36 (4) (1984) 515–521.

[8] K. Kitamura, A. Mitsuishi, T. Suzuki, F. Kimura, Fluid flow and heat transfer of natural convection induced around a vertical row of heated horizontal cylinders, Int. J. Heat Mass Tran. 92 (2016) 414–429.

[9] K. Kitamura, F. Kami-Iwa, T. Misumi, Heat transfer and fluid flow of natural convection around large horizontal cylinders, Int. J. Heat Mass Tran. 42 (22) (1999) 4093–4106.

[10] S. Grafsronningen, A. Jensen, Natural convection heat transfer from two horizontal cylinders at high Rayleigh numbers, Int. J. Heat Mass Tran. 55 (21–22) (2012) 5552–5564.

[11] S. Grafsrønningen, A. Jensen, B.A.P. Reif, PIV investigation of buoyant plume from natural convection heat transfer above a horizontal heated cylinder, Int. J. Heat Mass Tran. 54 (23–24) (2011) 4975–4987.

[12] S. Grafsrønningen, A. Jensen, Simultaneous PIV/LIF measurements of a transitional buoyant plume above a horizontal cylinder, Int. J. Heat Mass Tran. 55 (15–16) (2012) 4195–4206.

[13] M.A. Atmane, V.S. Chan, D.B. Murray, Natural convection around a horizontal heated cylinder: the effects of vertical confinement, Int. J. Heat Mass Tran. 46 (19) (2003) 3661–3672.

[14] J.P. Kuehner, J.R. Pflug, F.A. Tessier Jr., A.M. Hamed, F.J.M. Marin, Velocity measurements in the free convection flow above a heated horizontal cylinder, Int. J. Heat Mass Tran. 55 (17–18) (2012) 4711–4723.

[15] J.P. Kuehner, A. Hamed, J.D. Mitchell, Experimental investigation of the free convection velocity boundary layer and plume formation region for a heated horizontal cylinder, Int. J. Heat Mass Tran. 82 (2015) 78–97.

[16] S. Kimura, A. Bejan, Mechanism for transition to turbulence in buoyant plume flow, Int. J. Heat Mass Tran. 26 (10) (1983) 1515–1532.

[17] K. Noto, K. Teramoto, T. Nakajima, Spectra and critical Grashof numbers for turbulent transition in a thermal plume, J. Thermophys. Heat Tran. 13 (1) (1999) 82–90.

[18] J.C. Elicer-Cortes, R. Contreras, D. Boyer, M. Pavageau, R.H. Hernandez, Temperature spectra from a turbulent thermal plume by ultrasound scattering, Exp. Therm. Fluid Sci. 28 (8) (2004) 803–813.

[19] J.C. Elicer-Cortes, J. Fuentes, A. Valencia, C. Baudet, Experimental study of transition to turbulence of a round thermal plume by ultrasound scattering, Exp. Therm. Fluid Sci. 20 (3–4) (2000) 137–149.

[20] T.H. Kuehn, R.J. Goldstein, Numerical solution to the Navier-Stokes equations for laminar natural convection about a horizontal isothermal circular cylinder, Int. J. Heat Mass Tran. 23 (7) (1980) 971–979.

[21] P. Wang, R. Kahawita, T. Nguyen, Numerical computation of the natural convection flow about a horizontal cylinder using splines, Numer. Heat Tran. 17 (2) (1990) 191–215.

[22] T. Saitoh, T. Sajiki, K. Maruhara, Bench mark solutions to natural convection heat transfer problem around a horizontal circular cylinder, Int. J. Heat Mass Tran. 36 (5) (1993) 1251–1259.

[23] G. Sebastian, S. Shine, Natural convection from horizontal heated cylinder with and without horizontal confinement, Int. J. Heat Mass Tran. 82 (2015) 325–334.

[24] K.C. Lin, Y. Bhosale, C.-Y.Z. Huang, 3D-CFD investigation into free convection flow above a heated horizontal cylinder: comparisons with experimental data, Appl. Therm. Eng. 120 (2017) 277–288.
[25] A. Kumar, J.B. Joshi, A.K. Nayak, P.K. Vijayan, 3D CFD simulation of air cooled condenser-I: natural convection over a circular cylinder, Int. J. Heat Mass Tran. 78 (2014) 1265–1283.
[26] M. Corcione, Correlating equations for free convection heat transfer from horizontal isothermal cylinders set in a vertical array, Int. J. Heat Mass Tran. 48 (17) (2005) 3660–3673.
[27] J. Liu, H. Liu, Q. Zhen, W.-Q. Lu, Numerical investigation of the laminar natural convection heat transfer from two horizontally attached horizontal cylinders, Int. J. Heat Mass Tran. 104 (2017) 517–532.
[28] A. Kumar, J.B. Joshi, A.K. Nayak, P.K. Vijayan, 3D CFD simulations of air cooled condenser-II: natural draft around a single finned tube kept in a small chimney, Int. J. Heat Mass Tran. 92 (2016) 507–522.
[29] G.H.R. Kefayati, H. Tang, Lattice Boltzmann simulation of viscoplastic fluids on natural convection in an inclined enclosure with inner cold circular/elliptical cylinders Chock for (Part I: one cylinder), Int. J. Heat Mass Tran. 123 (2018) 1138–1162.
[30] G.H.R. Kefayati, H. Tang, MHD thermosolutal natural convection and entropy generation of Carreau fluid in a heated enclosure with two inner circular cold cylinders, using LBM, Int. J. Heat Mass Tran. 126 (2018) 508–530.
[31] G.R. Kefayati, H. Tang, Lattice Boltzmann simulation of viscoplastic fluids on natural convection in inclined enclosure with inner cold circular/elliptical cylinders (Part II: two cylinders), Int. J. Heat Mass Tran. 123 (2018) 1163–1181.
[32] G.R. Kefayati, H. Tang, Double-diffusive natural convection and entropy generation of Carreau fluid in a heated enclosure with an inner circular cold cylinder (Part I: heat and mass transfer), Int. J. Heat Mass Tran. 120 (2018) 731–750.
[33] G.R. Kefayati, H. Tang, Lattice Boltzmann simulation of viscoplastic fluids on natural convection in inclined enclosure with inner cold circular/elliptical cylinders (Part III: four cylinders), Int. J. Heat Mass Tran. 123 (2018) 1182–1203.
[34] S.B. Pope, Turbulent Flows, IOP Publishing, 2001.
[35] M. Pham, F. Plourde, K. Doan, Direct and large-eddy simulations of a pure thermal plume, Phys. Fluids 19 (12) (2007) 125103.
[36] J. Slotnick, A. Khodadoust, J. Alonso, D. Darmofal, W. Gropp, E. Lurie, D. Mavriplis, CFD Vision 2030 Study: a Path to Revolutionary Computational Aerosciences, NASA/CR-2014-218178, 2014.
[37] F.R. Menter, R.B. Langtry, S.R. Likki, Y.B. Suzen, P.G. Huang, S. Volker, A correlation-based transition model using local variables - Part I: model formulation, J. Turbomach. 128 (3) (2006) 413–422.
[38] D.K. Walters, D. Cokljat, A three-equation eddy-viscosity model for Reynolds-averaged Navier-Stokes simulations of transitional flow, J. Fluid Eng. 130 (12) (2008).
[39] B. Farouk, S. Güceri, Natural convection from a horizontal cylinder—turbulent regime, J. Heat Tran. 104 (2) (1982).
[40] Q. Pelletier, D.B. Murray, T. Persoons, Unsteady natural convection heat transfer from a pair of vertically aligned horizontal cylinders, Int. J. Heat Mass Tran. 95 (2016) 693–708.
[41] H.-T. Chen, Y.-J. Chiu, C.-S. Liu, J.-R. Chang, Numerical and experimental study of natural convection heat transfer characteristics for vertical annular finned tube heat exchanger, Int. J. Heat Mass Tran. 109 (2017) 378–392.
[42] H.-T. Chen, H.-Y. Chou, H.-C. Tseng, J.-R. Chang, Numerical study on natural convection heat transfer of annular finned tube heat exchanger in chimney with experimental data, Int. J. Heat Mass Tran. 127 (2018) 483–496.
[43] H.-T. Chen, Y.-L. Hsieh, P.-C. Chen, Y.-F. Lin, K.-C. Liu, Numerical simulation of natural convection heat transfer for annular elliptical finned tube heat exchanger with experimental data, Int. J. Heat Mass Tran. 127 (2018) 541–554.
[44] H.-T. Chen, Y.-S. Lin, P.-C. Chen, J.-R. Chang, Numerical and experimental study of natural convection heat transfer characteristics for vertical plate fin and tube heat exchangers with various tube diameters, Int. J. Heat Mass Tran. 100 (2016) 320–331.
[45] H.-T. Chen, W.-X. Ma, P.-Y. Lin, Natural convection of plate finned tube heat exchangers with two horizontal tubes in a chimney: experimental and numerical study, Int. J. Heat Mass Tran. 147 (2020).
[46] S. Grafsronningen, A. Jensen, Unsteady Reynolds averaged Navier-Stokes simulations of a buoyant plume above a cylinder, Proceed. Institution Civil Eng. Eng. Comput. Mech. 168 (1) (2015) 35–42.
[47] T. Léonard, L.Y. Gicquel, N. Gourdain, F. Duchaine, Steady/unsteady Reynolds-averaged Navier–Stokes and large eddy simulations of a turbine blade at high subsonic outlet mach number, J. Turbomach. 137 (4) (2015).
[48] N. Gourdain, F. Sicot, F. Duchaine, L. Gicquel, Large eddy simulation of flows in industrial compressors: a path from 2015 to 2035, Phil. Trans. Math. Phys. Eng. Sci. 372 (2022) (2014) 20130323.
[49] J.D. Denton, Some limitations of turbomachinery CFD, in: ASME Turbo Expo, Glasgow, UK, 2010.
[50] L. He, J. Yi, Two-scale methodology for URANS/large eddy simulation solutions of unsteady turbomachinery flows, J. Turbomach. 139 (10) (2017).
[51] S. Grafsrønningen, A. Jensen, Large eddy simulations of a buoyant plume above a heated horizontal cylinder at intermediate Rayleigh numbers, Int. J. Therm. Sci. 112 (2017) 104–117.
[52] R.J.M. Bastiaans, C.C.M. Rindt, F.T.M. Nieuwstadt, A.A. van Steenhoven, Direct and large-eddy simulation of the transition of two- and three-dimensional plane plumes in a confined enclosure, Int. J. Heat Mass Tran. 43 (13) (2000) 2375–2393.
[53] D.D. Gray, A. Giorgini, The validity of the Boussinesq approximation for liquids and gases, Int. J. Heat Mass Tran. 19 (5) (1976) 545–551.
[54] T.M. Eidson, Numerical simulation of the turbulent Rayleigh-Benard problem using subgrid modelling, J. Fluid Mech. 158 (1985) 245–268.
[55] J. Smagorinsky, General circulation experiments with the primitive equations: I. The basic experiment, Mon. Weather Rev. 91 (3) (1963) 99–164.
[56] M. Germano, U. Piomelli, P. Moin, W.H. Cabot, A dynamic subgrid-scale eddy viscosity model, Phys. Fluid. Fluid Dynam. 3 (7) (1991) 1760–1765.
[57] J. Worthy, Large Eddy Simulation of Buoyant Plumes, PhD, Cranfield University, 2003.
[58] G.K. Batchelor, Small-scale variation of convected quantities like temperature in turbulent fluid. Part 1: general discussion and the case of small conductivity, J. Fluid Mech. 5 (1) (1959) 113–133.
[59] J.-H. Heo, M.-S. Chae, B.-J. Chung, Influences of vertical and horizontal pitches on the natural convection of two staggered cylinders, Int. J. Heat Mass Tran. 57 (1) (2013) 1–8.
[60] B.J. Devenish, G.G. Rooney, D.J. Thomson, Large-eddy simulation of a buoyant plume in uniform and stably stratified environments, J. Fluid Mech. 652 (2010) 75–103.
[61] S. Narayan, A.K. Singh, A. Srivastava, Interferometric study of natural convection heat transfer phenomena around array of heated cylinders, Int. J. Heat Mass Tran. 109 (2017) 278–292.
[62] R.G. Bill Jr., B. Gebhart, The transition of plane plumes, Int. J. Heat Mass Tran. 18 (4) (1975) 513–526.
[63] E. Padilla, A. Silveira-Neto, Large-eddy simulation of transition to turbulence in natural convection in a horizontal annular cavity, Int. J. Heat Mass Tran. 51 (13–14) (2008) 3656–3668.
[64] H. Tennekes, J.L. Lumley, A First Course in Turbulence, The MIT Press, 1972.
[65] A. Shabbir, W.K. George, Experiments on a round turbulent buoyant plume, J. Fluid Mech. 275 (1994) 1–32.